



Designer meron lattice on the surface of a topological insulator

Daniele Guerzi ¹, Jie Wang,¹ J. H. Pixley,^{2,1} and Jennifer Cano ^{3,1}

¹*Center for Computational Quantum Physics, Flatiron Institute, New York, New York 10010, USA*

²*Department of Physics and Astronomy, Center for Materials Theory, Rutgers University, Piscataway, New Jersey 08854, USA*

³*Department of Physics and Astronomy, Stony Brook University, Stony Brook, New York 11974, USA*



(Received 23 May 2022; revised 5 December 2022; accepted 6 December 2022; published 15 December 2022)

We present a promising route to realize spontaneous magnetic order on the surface of a 3D topological insulator by applying a superlattice potential. The superlattice potential lowers the symmetry of the surface states and creates tunable van Hove singularities, which, when combined with strong spin-orbit coupling and Coulomb repulsion, give rise to a topological meron lattice spin texture. The periodicity of this designer meron lattice can be tuned by varying the periodicity of the superlattice potential. We employ Ginzburg-Landau theory to classify the different magnetic orders and show that the magnetic transition temperature reaches experimentally accessible values. Our work introduces another direction to realize exotic quantum order by engineering interacting Dirac electrons in a superlattice potential, with promising applications to spintronics.

DOI: [10.1103/PhysRevB.106.245417](https://doi.org/10.1103/PhysRevB.106.245417)

I. INTRODUCTION

Three-dimensional topological insulators (TIs) host gapless surface Dirac cones protected by time-reversal symmetry [1–11]. In the presence of strong interactions, time-reversal symmetry can be spontaneously broken, gapping the Dirac cone. The result is an exotic magnetically ordered surface exhibiting the quantized anomalous Hall effect [5,12–18]. However, for all measured TIs, the Coulomb interaction is too weak to induce the magnetically ordered phase [5,12,14,18].

In this paper, we show that a superlattice potential enhances correlation effects and provides an experimentally accessible route to realize spontaneous magnetic order on the surface of a TI as depicted in Fig. 1(a). The superlattice potential downfolds and strongly renormalizes the low-energy band structure, creating satellite Dirac cones without opening a gap [19] and inducing strong van Hove singularities (VHSs) [20]. We show that the superlattice-induced VHSs drive a spin density wave instability that results in an exotic meron lattice taking place at arbitrarily small values of the electron-electron interaction. A meron, as shown in Fig. 1(b), is topologically equivalent to half a skyrmion: Magnetic moments in its core point up or down, but magnetic moments along its boundary are in-plane [21]. While topological spin textures such as skyrmions have been observed in noncentrosymmetric magnets [22–25], ultrathin magnetic films [26–28] and multiferroic insulators [29,30], a meron lattice has only been observed recently [31,32].

The meron lattice we describe on the surface of the TI is stabilized by the interplay between the superlattice potential and the strong spin-orbit coupling (SOC) on the TI surface that “locks” the spin to the momentum, forcing the magnetic moments to rotate in space about an in-plane axis. It features several novel aspects: (1) it leaves the surface Dirac cone gapless; (2) each unit cell exhibits two merons with opposite

topological charge; and (3) the meron lattice periodicity is determined by the applied potential, i.e., it can be chosen by design. These features make it distinct from other magnetic textures induced on [5,12–18] or proximity-coupled [33–37] to the surface of a TI.

In this work we focus on the experimental setup shown in Fig. 1(a), which depicts a superlattice potential imposed on the surface of a TI by gating a patterned dielectric stacked above the TI surface. This approach was introduced to realize a superlattice potential on graphene with periodicity down to 35 nm and strength ~ 50 meV [38,39]. It offers great tunability: The periodicity, strength, and symmetry of the potential can be engineered. A superlattice potential has been studied theoretically to band-engineer topological materials [19,20,40–49]. Strain has also been employed to modify the dispersion of surface states [50,51].

II. MODEL OF AN INTERACTING TI SURFACE

We consider interacting electrons on the surface of a TI described by the Hamiltonian $\hat{H} = \hat{H}_0 + \hat{H}_{\text{int}}$. The noninteracting Hamiltonian $\hat{H}_0 = \int d^2\mathbf{r} \hat{\Psi}^\dagger(\mathbf{r}) H_0(\mathbf{r}) \hat{\Psi}(\mathbf{r})$ describes a spin-momentum-locked Dirac cone subject to a superlattice potential,

$$H_0(\mathbf{r}) = v_F(-i\nabla_{\mathbf{r}} \times \boldsymbol{\sigma})_z + \sigma_0 w(\mathbf{r}), \quad (1)$$

where $\nabla_{\mathbf{r}} = (\partial_x, \partial_y)$, $\boldsymbol{\sigma} = (\sigma_x, \sigma_y, \sigma_z)$ are the Pauli matrices, σ_0 is the identity, and $w(\mathbf{r}) = 2w \sum_{j=1}^3 \cos(\mathbf{q}_j \cdot \mathbf{r})$ is the hexagonal superlattice potential, with amplitude $2w$ and wave vectors $\mathbf{q}_{1,2,3}$ illustrated as red vectors in Fig. 2(a). The wave vectors satisfy $|\mathbf{q}_{1,2,3}| = 4\pi/\sqrt{3}L$, where L is the periodicity of the potential. We set the Fermi velocity to $v_F = 2.55$ eV Å, the experimentally measured value in Bi₂Te₃ [7,8]. For the moment we neglect higher-order corrections [5] to the Dirac

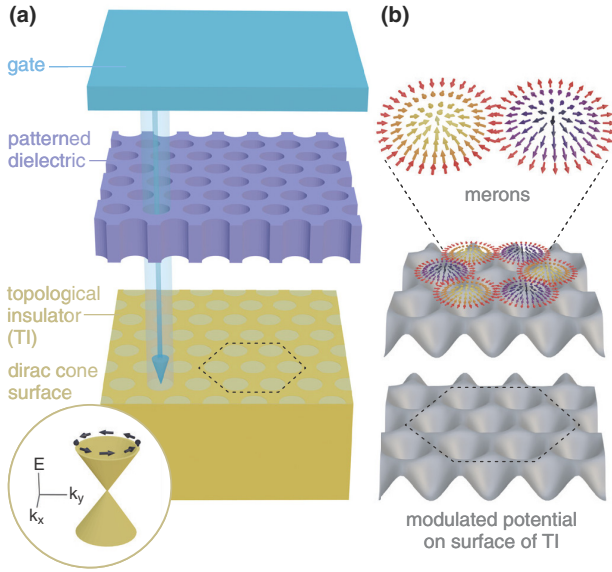


FIG. 1. Schematic of experiment and meron spin texture. (a) The experiment consists, from top to bottom, of a metallic gate, a patterned dielectric, and a topological insulator. Applying a bias between the metallic gate and the topological insulator imposes a modulated potential on the surface of the TI. (b) Magnetization exhibiting half-integer winding characteristic of a meron spin texture. Merons pinned by the superlattice potential form a meron lattice.

cone dispersion (1). Then Eq. (1) depends only on a single dimensionless parameter $w/(v_F/L)$.

The superlattice potential has a profound effect on the Dirac cone. The dispersion of the first band above charge neutrality [red line in Fig. 2(b)] becomes nearly flat at the \mathbf{K} and \mathbf{K}' points of the moiré Brillouin zone. Specifically, near \mathbf{K} and \mathbf{K}' , symmetry constrains the Taylor expansion of the dispersion to the form $\epsilon_{\pm}(\mathbf{k}) = \alpha k^2 \pm \eta(k_x^3 - 3k_x k_y^2)$, where \pm indicates valley; expressions for the coefficients α and η are given in Appendix A. This yields three VHSs near \mathbf{K} and \mathbf{K}' that map onto each other under C_{3z} and provide the large diverging density of states (DOS) shown in Fig. 2(c). In addition, there is a local maximum (minimum) for $\alpha < 0$ (> 0) at $\mathbf{k} = 0$. At a critical value of $w/(v_F/L)$ where $\alpha = 0$, the three nearby VHSs merge to form higher-order VHSs at \mathbf{K} and \mathbf{K}' with a power-law diverging DOS [52–55], as found in Ref. [20]. Our results do not require fine-tuning to the critical value of $w/(v_F/L)$. Instead, we focus on the vicinity of the VHSs that produce a sharp peak in the DOS [highlighted by the horizontal line in Fig. 2(b)].

To describe the magnetic instability with momentum $\mathbf{K}' - \mathbf{K}$ we consider the electron-electron interaction coupling the hot-spot regions around \mathbf{K} and \mathbf{K}' . Note that screening by low-energy electrons at momentum transfer $\mathbf{q} = \mathbf{K}' - \mathbf{K}$ is weak because electrons at \mathbf{K} and \mathbf{K}' occupy orthogonal Bloch states (see discussion at the end of Appendix C).

For simplicity we focus on the Hubbard interaction:

$$\hat{H}_{\text{int}} = U \int d^2\mathbf{r} \hat{\Psi}_{\uparrow}^{\dagger}(\mathbf{r}) \hat{\Psi}_{\downarrow}^{\dagger}(\mathbf{r}) \hat{\Psi}_{\downarrow}(\mathbf{r}) \hat{\Psi}_{\uparrow}(\mathbf{r}), \quad U > 0, \quad (2)$$

where $\hat{\Psi}_{\uparrow, \downarrow}(\mathbf{r})$ is the electron annihilation operator, $\hat{\Psi}_{\sigma}(\mathbf{r}) = \sum_{\mathbf{k}, \mathbf{G}} e^{i(\mathbf{k}-\mathbf{G})\mathbf{r}} \hat{c}_{\mathbf{k}, \mathbf{G}, \sigma} / \sqrt{A}$ with A area of the sample, \mathbf{k} and \mathbf{G}

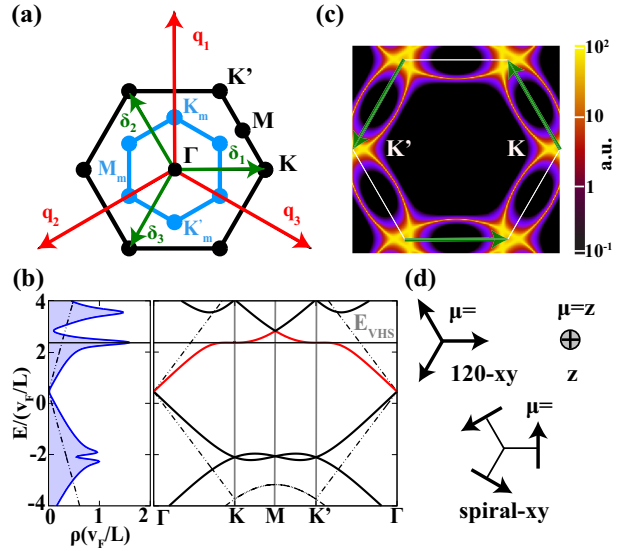


FIG. 2. Superlattice Brillouin zone, electronic properties of surface states, and magnetic ordering basis. (a) Black and cyan lines show the superlattice and magnetic Brillouin zones, respectively. The red and green arrows represent the wave vectors \mathbf{q}_j and the nesting vectors δ_j , respectively. (b) Density of states and electronic dispersion for $w/(v_F/L) \simeq 1.54$ ($L = 20$ nm, $w = 20$ meV). Dashed lines show the density of states and the band structure of the TI Dirac cone folded into the superlattice Brillouin zone. (c) Momentum-resolved spectral function displaying the Fermi surface at the energy of the VHS with $w/(v_F/L) \simeq 1.54$. (d) Decomposition of the order parameter into $\mathbf{v}_{\mu j}$.

label the Bloch momentum and reciprocal lattice vector of the moiré Brillouin zone, respectively, and $\hat{c}_{\mathbf{k}, \mathbf{G}, \sigma}^{\dagger}$ creates an electron at $\mathbf{k} - \mathbf{G}$ with spin σ . Notice that Ref. [20] considered an attractive interaction ($U < 0$) and found that the VHS enhances the superconducting critical temperature.

A. Spin density wave operators

The interaction term \hat{H}_{int} drives an instability toward density wave ordering, modulated by the nesting vectors, δ_j , which connect the \mathbf{K} and \mathbf{K}' regions where the DOS diverges at the VHS. The nesting vectors are indicated by green vectors in Figs. 2(a) and 2(c), and define a magnetic Brillouin zone [solid cyan line in Fig. 2(a)] three times smaller than the original one. Spin-momentum locking is expected to drive the formation of an exotic spin density wave (SDW) [41]. To study the SDW, we decompose the order parameters for each modulation δ_j [5] into an in-plane direction parallel to the nesting vector, $\mathbf{v}_{\parallel j} = \mathbf{e}_j \equiv \delta_j/|\delta_j|$; an in-plane direction perpendicular to the nesting vector, $\mathbf{v}_{\perp j} = -i(\mathbf{z} \times \mathbf{e}_j)$; and an out-of-plane part, $\mathbf{v}_{zj} = -i\mathbf{z}$. Correspondingly, for each wave vector δ_j , the SDW operator can be decomposed as

$$\hat{S}_{\mu j} = \sum_{\mathbf{k}} \sum_{\mathbf{G}} \hat{c}_{\mathbf{k}+\delta_j, \mathbf{G}, \sigma}^{\dagger} \mathbf{v}_{\mu j} \cdot \boldsymbol{\sigma}_{\sigma\sigma'} \hat{c}_{\mathbf{k}, \mathbf{G}, \sigma'}, \quad (3)$$

which represents the three types of magnetic order illustrated in Fig. 2(d). We observe that we have 9 independent spin density waves corresponding to different combinations of δ_j and $\mathbf{v}_{\mu j}$.

TABLE I. Symmetries of the SDW operator $\hat{S}_{\mu j}$ playing a key role in determining the Ginzburg-Landau free energy. The transformation m_y acts differently on $\mu = \parallel, z$ and \perp .

SDW	C_{3z}	m_x	T	m_y
$\hat{S}_{\mu 1}$	$\hat{S}_{\mu 2}$	$\hat{S}_{\mu 1}^\dagger$	$-\hat{S}_{\mu 1}^\dagger$	If z, \parallel : $-\hat{S}_{\mu 1}$; else $\hat{S}_{\perp 1}$
$\hat{S}_{\mu 2}$	$\hat{S}_{\mu 3}$	$\hat{S}_{\mu 3}^\dagger$	$-\hat{S}_{\mu 2}^\dagger$	If z, \parallel : $-\hat{S}_{\mu 3}$; else $\hat{S}_{\perp 3}$
$\hat{S}_{\mu 3}$	$\hat{S}_{\mu 1}$	$\hat{S}_{\mu 2}^\dagger$	$-\hat{S}_{\mu 3}^\dagger$	If z, \parallel : $-\hat{S}_{\mu 2}$; else $\hat{S}_{\perp 2}$

B. Symmetries

The interacting Hamiltonian \hat{H} composed by \hat{H}_0 (1) and \hat{H}_{int} (2) is invariant under time-reversal $T = \sigma_y K$, where K indicates complex conjugation, as well as a threefold rotational symmetry, $C_{3z} = e^{i\pi\sigma_z/3}$, and the mirror symmetries, $m_y = i\sigma_y$ and $m_x = i\sigma_x$, which act on both spin and spatial coordinates. Combinations of these imply invariance under two- and sixfold rotation symmetries, $C_{2z} = i\sigma_z$, $C_{6z} = e^{i\pi\sigma_z/6}$, respectively. In order to determine the leading spin density wave instability it is crucial to notice that the Bloch states $|u_{\mathbf{K}}\rangle$ and $|u_{\mathbf{K}'}\rangle$ of the Hamiltonian (1) at the hot spots are singly degenerate and have opposite mirror m_y eigenvalues. This can be readily understood observing that the time-reversal symmetry T sends $\mathbf{K} \rightarrow \mathbf{K}'$ and $T m_y T^{-1} = m_y$. Thus, given $|u_{\mathbf{K}}\rangle$ with $m_y |u_{\mathbf{K}}\rangle = i |u_{\mathbf{K}}\rangle$, it follows that $m_y |u_{\mathbf{K}'}\rangle = m_y T |u_{\mathbf{K}}\rangle = -iT |u_{\mathbf{K}}\rangle = -i |u_{\mathbf{K}'}\rangle$. The potential $w(\mathbf{r})$ breaks particle-hole symmetry. The action of the symmetries of the model on the spin density wave operators $\hat{S}_{\mu j}$ is illustrated in Table I.

III. GINZBURG-LANDAU MEAN-FIELD THEORY

We study the magnetic order by deriving a Ginzburg-Landau theory. We decouple the local interaction (2) introducing the Hubbard-Stratonovich fields $n(\mathbf{r}, \tau)$ and $\mathbf{m}(\mathbf{r}, \tau)$ [56–58] for the charge and the magnetization densities to obtain the Lagrangian:

$$\mathcal{L} = \int d^2\mathbf{r} \bar{\Psi}(\partial_\tau + H_0(\mathbf{r}) - \mu)\Psi + \frac{U}{2} \int d^2\mathbf{r} [n\rho - \mathbf{m} \cdot \mathbf{S}] + \frac{U}{4} \int d^2\mathbf{r} [\mathbf{m}^2 - n^2], \quad (4)$$

where for the sake of space we omit the dependencies of the fields on the imaginary time τ and position \mathbf{r} , and we have introduced the fermionic operators $\hat{\rho}(\mathbf{r}) = \sum_\sigma \hat{\Psi}_\sigma^\dagger(\mathbf{r})\hat{\Psi}_\sigma(\mathbf{r})$ and $\hat{S}_a(\mathbf{r}) = \hat{\Psi}^\dagger(\mathbf{r})\sigma_a\hat{\Psi}(\mathbf{r})$. Integrating out the electronic degrees of freedom of Eq. (4) we obtain the effective action for $n(\tau, \mathbf{r})$ and $\mathbf{m}(\mathbf{r}, \tau)$. Then, we take the semiclassical limit of a static order parameter. More specifically, we assume a homogenous electron density n and a spatially modulated magnetization $\mathbf{m}(\mathbf{r}) = \sum_{j=1}^3 (\mathbf{m}_{\delta_j} e^{i\delta_j \mathbf{r}} + \mathbf{m}_{-\delta_j} e^{-i\delta_j \mathbf{r}})$ where \mathbf{m}_{δ_j} is the Fourier amplitude associated to the modulation δ_j . Since $\mathbf{m}(\mathbf{r})$ is real, $\mathbf{m}_{\delta_j} = \mathbf{m}_{-\delta_j}^* \equiv \mathbf{m}_j$. We expand $\mathbf{m}_j = \sum_\mu s_{\mu j} \mathbf{v}_{\mu j}$ where $\mathbf{v}_{\mu j}$ are the normal modes in Fig. 2(d) and the order parameter $s_{\mu j} = \langle \hat{S}_{\mu j} \rangle / A$ is the average value of $\hat{S}_{\mu j}$ with A area of the

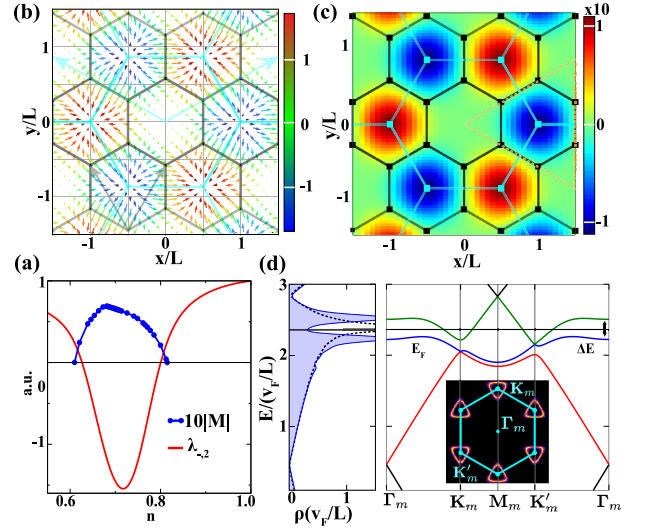


FIG. 3. Saddle-point solution, real-space magnetization, and electronic structure in the meron lattice phase. (a) Blue and red data show the total magnetization $|M|$ and the lowest eigenvalue of $\mathcal{M}_{jl}^{\mu\nu}$, respectively. (b) Contour plot of the magnetization in real space. Color indicates the out-of-plane component. (c) Winding number $\mathbf{m} \cdot (\partial_x \mathbf{m} \times \partial_y \mathbf{m}) / 4\pi$ in real space. Black and cyan lines show the superlattice and magnetic unit cells, respectively. (d) Density of states and electronic dispersion of the meron lattice state. The dashed line shows the density of states of the normal phase. The horizontal line shows the Fermi energy E_F ; ΔE denotes the induced gap at Γ_m . Inset shows the Fermi surface of the magnetic state. The bands are obtained from the Hartree-Fock solution at $w/(v_F/L) \simeq 1.54$, $2w = 40$ meV, $U = 30$ meV, and $T = 1.5$ K.

sample. As a result we find the free energy:

$$F = \frac{A}{2} \left(\sum_{\mu j} |s_{\mu j}|^2 - \frac{n^2}{2} \right) + \sum_{m=1}^{\infty} \text{Tr} \left[\frac{(-G_0 X)^m}{m U} \right], \quad (5)$$

where $G_0 = (-\partial_\tau - H_0 + \mu)^{-1}$ is the noninteracting single-particle Green's function and $X = U \mathbf{m}(\mathbf{r}) \cdot \boldsymbol{\sigma} / 2 - U n / 2$ describes the interaction between the order parameter and the electrons.

The self-consistency equations are obtained by minimizing the free energy (5) with respect to the variational parameters n and $s_{\mu j}$, i.e., $\delta F / \delta n = 0$ and $\delta F / \delta s_{\mu j} = 0$. The magnetic order is determined by finding the roots of these equations numerically, as detailed in Appendix B. We find that in the range of filling between $n \sim 0.61$ and $n \sim 0.8$ the minimum of the free energy (5) develops a SDW magnetic ordering. The blue data in Fig. 3(a) show the magnitude of the total magnetization density, $|M| = \sqrt{\sum_{\mu j} |s_{\mu j}|^2}$, as a function of the filling per unit cell of the superlattice.

In real space, the magnetic order $\mathbf{m}(\mathbf{r})$ obtained from the saddle-point solution forms a Néel-type meron lattice [25] with two merons in each unit cell, as shown in Fig. 3(b). The merons are well defined because the magnetic moment is forced to be in-plane along mirror-invariant lines. Each meron can be characterized by the Pontryagin density $\Phi(\mathbf{r}) = \hat{\mathbf{m}}(\mathbf{r}) \cdot [\partial_x \hat{\mathbf{m}}(\mathbf{r}) \times \partial_y \hat{\mathbf{m}}(\mathbf{r})] / 4\pi$ shown in Fig. 3(c) where $\hat{\mathbf{m}}$ is a unit magnetization vector. We find $\int_S d^2\mathbf{r} \Phi(\mathbf{r}) = \pm 1/2$, where S

is the triangular domain illustrated by the orange dashed line in Fig. 3(c). In the center of each unit cell is an intermediate region of destructive interference with vanishing magnetization. The magnetic order spontaneously breaks the translation symmetry of the potential, giving rise to a magnetic unit cell [cyan line in Fig. 3(b)] three times larger ($\sqrt{3} \times \sqrt{3}$) than the original one [black solid line in Fig. 3(b)].

Hartree-Fock Hamiltonian

In this section we discuss the properties of the electronic band structure in the magnetic phase. We treat the effect of the magnetization on the electronic spectrum at the Hartree-Fock level by replacing $H_0(\mathbf{r})$ in Eq. (1) with

$$H_{\text{HF}}(\mathbf{r}) = H_0(\mathbf{r}) - \frac{U}{2} \mathbf{m}(\mathbf{r}) \cdot \boldsymbol{\sigma}. \quad (6)$$

Despite breaking time-reversal symmetry, the resulting electronic spectrum remains gapless because the magnetic order preserves $C_{2z}T$ symmetry. The dispersion is plotted in the right panel of Fig. 3(d) in the magnetic Brillouin zone: The original red band in Fig. 2(b) is decomposed into three different bands given by the red, blue, and green lines in Fig. 3(d). The Dirac cones at \mathbf{K}_m between the red and blue bands and at \mathbf{K}'_m between the blue and the green ones are protected by $C_{2z}T$. Thus, they give rise to a gapless electronic spectrum whose Fermi surface is shown in the inset of Fig. 3(d).

Although the order parameter $\mathbf{m}(\mathbf{r})$ does not open a full gap, it significantly reduces the DOS at the Fermi level [horizontal black dashed line in Fig. 3(d)] by opening a gap between the blue and green bands at Γ_m of order $\Delta E \propto U|M|$. The gap splits the peak in the DOS resulting from the VHS into two peaks above and below, as shown in the left panel of Fig. 3(d). The significant decrease in the kinetic energy from splitting the large peak in the DOS makes the magnetic state energetically favorable with respect to the normal one.

In the following we discuss the symmetries of the magnetic phase and we determine the region of stability of the spin density wave order.

IV. PHASE DIAGRAM

The instability of the Dirac cone surface state is determined by expanding the free energy for small values of the order parameter $s_{\mu j}$. As time-reversal symmetry acts on the order parameter by $T : s_{\mu j} \rightarrow -s_{\mu j}^*$ (see Table I), only even powers of $s_{\mu j}$ are allowed in the free energy (5), so that to second order in $s_{\mu j}$ at fixed density n , $F_{(2)} = \sum_{\mu\nu} \sum_{jl=1}^3 s_{\mu j}^* \mathcal{M}_{jl}^{\mu\nu} s_{\nu l} / 2$, where

$$\mathcal{M}_{jl}^{\mu\nu} = \delta_{\mu\nu} \delta_{jl} - \frac{U}{2} \chi_{jl}^{\mu\nu}, \quad (7)$$

and $\chi_{jl}^{\mu\nu} \equiv \int_0^\beta d\tau \langle \hat{s}_{\mu j}^\dagger(\tau) \hat{s}_{\nu l}(0) \rangle / A$ is the thermodynamic spin susceptibility with τ imaginary time and β inverse temperature. The matrix $\mathcal{M}_{jl}^{\mu\nu}$ contains both diagonal terms ($j = l$), which come from momentum-conserving scattering processes, and off-diagonal terms ($j \neq l$) from umklapp processes with momentum $\delta_j - \delta_l \in \mathbf{G}$ with \mathbf{G} a reciprocal lattice vector. The matrix $\mathcal{M}_{jl}^{\mu\nu}$ is constrained by the symmetries of the Hamiltonian as discussed in Appendix C.

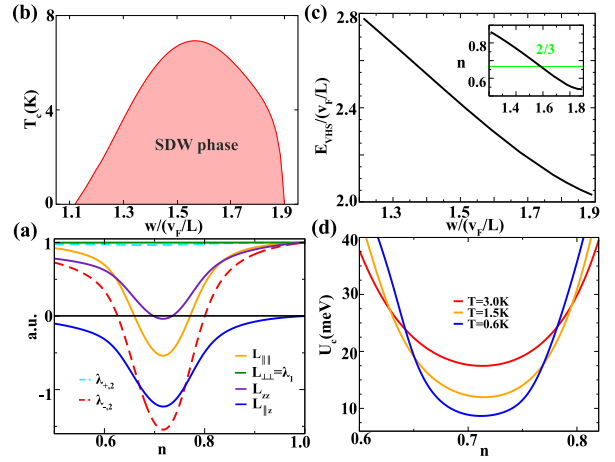


FIG. 4. Magnetic instability, critical temperature, and interaction. (a) Solid lines show the components of the second-order free energy $L_{\mu\nu}$. Red and cyan dashed lines illustrate the eigenvalues $\lambda_{-,2}$ and $\lambda_{+,2}$, respectively, while $\lambda_1 = L_{\perp\perp}$ is the solid green line. The calculations were performed at $T = 1.5$ K, $U = 30$ meV, and $w/(v_F/L) \simeq 1.54$. (b) Critical temperature for the magnetic transition as a function of $w/(v_F/L)$ for $U = 30$ meV. For a given $w/(v_F/L)$, the filling n is set so that the Fermi level is at the energy of the VHS. (c) Evolution of the energy of the VHS singularity as a function of $w/(v_F/L)$. Inset shows the electron filling per superlattice unit cell at the VHS versus $w/(v_F/L)$. (d) Critical interaction U_c as a function of the filling n at several temperatures, fixing $2w = 40$ meV and $w/(v_F/L) \simeq 1.54$.

An instability exists when one of the eigenvalues of the matrix $\mathcal{M}_{jl}^{\mu\nu}$ becomes negative, which comprises a generalization of the Stoner criterion [59]. The corresponding eigenvector indicates the magnetic configuration of the instability and is classified by how it transforms under symmetry. Since the saddle-point solution is C_{3z} -symmetric, we consider a C_{3z} -invariant eigenvector of $\mathcal{M}_{jl}^{\mu\nu}$, which implies the magnetization takes the form $s_{\mu j} = MU_\mu / \sqrt{3}$. It follows that

$$F_{(2)} = \frac{|M|^2}{2} \begin{pmatrix} U_{\parallel} \\ U_{\perp} \\ U_z \end{pmatrix}^\dagger \begin{pmatrix} L_{\parallel\parallel} & 0 & L_{\parallel z} \\ 0 & L_{\perp\perp} & 0 \\ L_{\parallel z} & 0 & L_{zz} \end{pmatrix} \begin{pmatrix} U_{\parallel} \\ U_{\perp} \\ U_z \end{pmatrix}, \quad (8)$$

where the elements $L_{\mu\nu} = \sum_{jl} \mathcal{M}_{jl}^{\mu\nu} / 3$ are shown in Fig. 4(a) as a function of the density at $T = 1.5$ K. The perpendicular (U_{\perp}) component of the magnetic order is decoupled from the other components (U_{\parallel} , U_z) because it is even under the mirror m_y , while the parallel and z components are odd. This property can be readily understood by looking at the last column of Table I, where we show the action of the symmetry m_y on the different components of the spin density wave order. From Eq. (8), the surface Dirac cone is unstable when either $\lambda_1 = L_{\perp\perp} < 0$, which corresponds to in-plane order purely in the ‘‘spiral-xy’’ channel and even under m_y , or when one of the eigenvalues $\lambda_{\pm,2} = (L_{\parallel\parallel} + L_{zz})/2 \pm \sqrt{(L_{\parallel\parallel} - L_{zz})^2/4 + L_{\parallel z}^2} < 0$, which corresponds to a generically noncoplanar SDW with ‘‘120-xy’’ and z components, and breaking m_y [see Fig. 2(d)]. In order to characterize the magnetic instability we compute the spin susceptibility introduced

in Eq. (7):

$$\chi_{jl}^{\mu\nu} = -\frac{T}{A} \sum_{\mathbf{k}, \epsilon_n} \text{Tr}[G_0(\mathbf{k}, i\epsilon_n) O_{\mu j}^\dagger V^{\delta_j - \delta_l} G_0(\mathbf{k} + \delta_l, i\epsilon_n) O_{vl}], \quad (9)$$

where $G_0(\mathbf{k}, i\epsilon_n)$ is the single-particle Green's function

$$G_0(\mathbf{k}, i\epsilon) = \sum_n \frac{|u_{n\mathbf{k}}\rangle\langle u_{n\mathbf{k}}|}{i\epsilon - \xi_{n\mathbf{k}}}, \quad (10)$$

where $|u_{n\mathbf{k}}\rangle$ are the Bloch states of H_0 , for simplicity we have introduced the operator $O_{\mu j} = \mathbf{v}_{\mu j} \cdot \boldsymbol{\sigma}$, and $V^{\mathbf{G}}$ is the sewing matrix $V_{\mathbf{Q}, \mathbf{Q}'}^{\mathbf{G}} = \delta_{\mathbf{Q}, \mathbf{Q} + \mathbf{G}}$. We find that for a range of filling near $2/3$ electrons per unit cell, the dominant instability occurs in the channel corresponding to $\lambda_{-,2}$, as shown by the region where the red solid line in Fig. 3(a) goes negative, and in agreement with our saddle-point solution. This solution, which breaks m_y , is energetically favored over the in-plane spin solution that is even in m_y because it allows a gap to open at Γ_m in the magnetic BZ, indicated by ΔE in Fig. 3(d). Indeed, the latter solution being odd under m_y allows mixing between the Bloch states $|u_{\mathbf{K}}\rangle$ and $|u_{\mathbf{K}'}\rangle$ at the hot-spot regions which are characterized by opposite mirror m_y eigenvalues as detailed in Appendix C. The resulting magnetic state is a pattern of half-integer topological vortices, with the same winding and opposite polarities corresponding to a meron lattice. The other magnetic state, with eigenvalue $\lambda_{+,2}$, also breaks m_y , but is energetically unfavorable because it exhibits a clockwise magnetization winding inconsistent with the intrinsic SOC of the surface state in Eq. (1). We have also studied the C_{3z} -breaking magnetic orders. Since these orders do not hybridize the states $|u_{\mathbf{K}}\rangle$ and $|u_{\mathbf{K}'}\rangle$, they do not lead to a magnetic instability. The symmetry of the magnetic orders is further discussed in Appendix C.

The critical temperature and interaction strength occur at precisely the point where one of the eigenvalues of $\mathcal{M}_{jl}^{\mu\nu}$ changes sign. Figure 4(b) shows the critical temperature for a range of fillings around the VHS at $U = 30$ meV. The magnetic dome peaks at $T_c \sim 7$ K near an optimal value of $w/(v_F/L) \simeq 1.54$: Surprisingly, the peak does not coincide with the higher-order VHS [20] at $w/(v_F/L) \simeq 1.36$. Figure 4(c) shows the evolution of the energy and the number of electrons per superlattice unit cell where the VHS occurs as a function of $w/(v_F/L)$. The maximum critical temperature for the magnetic transition takes place around $n \sim 2/3$ filling, denoted as the horizontal green line in the inset of Fig. 4(c).

Figure 4(d) shows the critical interaction U_c necessary to induce the magnetic instability as a function of the filling n for different temperatures T . Lowering T reduces the magnetic transition to arbitrarily weak repulsive interactions. In contrast, in the absence of the superlattice potential, spontaneous magnetization of the surface state [5,12–18] in the Bi_2Se_3 family requires a critical value of the Coulomb interaction, on the order of 2 eV [13,14,18]. We expect our results are robust to weak disorder, which will reduce the transition temperature [60–62] without eliminating the magnetic state.

Hexagonal warping

Beyond the linear momentum dependence of the Dirac cone (1) the dispersion develops a hexagonal warping term

$H_w(\mathbf{k}) = \lambda(k_x^3 - 3k_x k_y^2)\sigma_z$ [5]. Despite being small in $\lambda/v_F L^2$ this correction gives rise to a series of interesting effects that are experimentally relevant. The hexagonal warping breaks m_y and $C_{2z}T$ symmetries which gives a finite U_\perp component in the magnetization pattern. While the average magnetic moment in the unit cell continues to vanish, $\int d^2\mathbf{r} m_i = 0$, the explicitly broken m_y symmetry gives rise to a finite out-of-plane toroidal moment $\mathcal{T}_z = \int d^2\mathbf{r} (xm_y - ym_x)/2$ [63–65] which typically manifests in the magnetoelectric susceptibility $\alpha_{xy} = -\alpha_{yx}$ [66,67].

V. CONCLUSIONS

We have shown that a superlattice potential on the surface of a TI provides a route to spontaneously breaking time-reversal symmetry on the TI surface. The magnetic order realizes a meron lattice exhibiting pairs of merons with opposite topological charge in the unit cell. The periodicity of the meron lattice is determined by the period of the potential; consequently, the meron lattice periodicity is completely tunable. Although the magnetic order breaks time-reversal, it preserves $C_{2z}T$ and thus does not open a gap on the TI surface.

The meron lattice phase can be measured by imaging the magnetization in real space through Lorentz transmission electron microscopy [26,68] and nitrogen vacancy magnetometry [69] or in reciprocal space via x-ray diffraction [22,70–75]. The magnetization can also be measured through the magneto-optical Kerr effect [76,77] and reflective magnetic circular dichroism [78]. In addition, the magnetoelectric susceptibility α_{xy} is observed either by measuring an in-plane magnetization in response to an electric field, or a current resulting from an in-plane magnetic field. The reduced density of states resulting from the magnetic order gives a drastic variation of the electronic compressibility across the transition. Finally, we also expect that the response to a magnetic field [79–85] gives rise to distinctive signatures of the meron state.

This finding has far-reaching consequences, as this unconventional magnetic state will have implications both on the experimental and on the theoretical level. First, the topological spin texture realizes an electromagnetic field on the scale of the superlattice that can be employed by proximity effects to modify band structure and topological properties of electronic systems [33,35,37,86–89]. Second, the broken mirror symmetry that results from hexagonal warping of the Fermi surface implies that the meron lattice might host a magnetoelectric response with potential application to spintronics [88–93]. This effect can be enhanced by strain [94–96] and lattice relaxation [97]. Finally, the interplay between the spin density wave ordering and possible superconducting instabilities [20] is an open problem which is left to future studies.

ACKNOWLEDGMENTS

We have benefited from discussions with Y.-Z. Chou, M. Michael Denner, S. Fang, J. Zang, A. J. Millis, Zhentao Wang, Tiancheng Song, and Justin Wilson. We are grateful to Lucy Reading-Ikkanda for creating the figure of the experimental setup and the sketch of the magnetic state. We also acknowledge the support of the Flatiron Institute, a division of the

Simons Foundation. This work was partially supported by the Air Force Office of Scientific Research under Grant No. FA9550-20-1-0260 (J.C.) and Grant No. FA9550-20-1-0136 (J.H.P.) and the Alfred P. Sloan Foundation through a Sloan Research Fellowship (J.H.P.). J.H.P. and J.C. acknowledge hospitality of the Aspen Center for Physics, where some of this work was developed and which is supported by National Science Foundation Grant No. PHY1607611.

APPENDIX A: THE $\mathbf{k} \cdot \mathbf{p}$ EXPANSION AROUND \mathbf{K} AND \mathbf{K}'

The origin of the high-order van Hove singularities [52–55] can be derived from the lattice symmetries of the Hamiltonian $H_0(\mathbf{r})$. We define the small deviation from the \mathbf{K} point, $\mathbf{q} = \mathbf{k} - \mathbf{K}$, and the linear combinations $q_{\pm} = q_x \pm iq_y$, which transform under C_{3z} as $q_{\pm} \rightarrow e^{\pm i2\pi/3} q_{\pm}$. At second order in \mathbf{q} the only allowed term in the energy dispersion is $q_+ q_- = q^2$. The next contributions invariant under C_{3z} are q_+^3 and q_-^3 . As a consequence of the mirror m_y symmetry the cubic term is $(q_+^3 + q_-^3)/2 = q_x^3 - 3q_y^2 q_x$. Thus, to cubic order in \mathbf{q} the dispersion around \mathbf{K} reads [20] $\epsilon_{\mathbf{K}}(\mathbf{q}) = \epsilon_0 + \alpha q^2 + \eta(q_x^3 - 3q_x q_y^2) + \dots$. Applying time-reversal symmetry we find that the expansion at \mathbf{K}' reads $\epsilon_{\mathbf{K}'}(\mathbf{q}) \simeq \epsilon_0 + \alpha q^2 - \eta(q_x^3 - 3q_x q_y^2)$. The values of the coefficients α and η are obtained from the $\mathbf{k} \cdot \mathbf{p}$ perturbation theory at \mathbf{K} . Given $H_0(\mathbf{K} + \mathbf{q}) - H_0(\mathbf{K})$, expanding to the third order in the small deviation $\mathbf{q} = \mathbf{k} - \mathbf{K}$ yields

$$\alpha = 2 \sum_{m \neq n} \frac{\text{Re}[\langle u_{n\mathbf{K}} | \sigma_+ | u_{m\mathbf{K}} \rangle \langle u_{m\mathbf{K}} | \sigma_- | u_{n\mathbf{K}} \rangle]}{\epsilon_{n\mathbf{K}} - \epsilon_{m\mathbf{K}}} \quad (\text{A1})$$

and

$$\eta = \sum_{m, j \neq n} 2 \text{Im} \left[\frac{\langle u_{n\mathbf{K}} | \sigma_- | u_{m\mathbf{K}} \rangle \langle u_{m\mathbf{K}} | \sigma_- | u_{j\mathbf{K}} \rangle \langle u_{j\mathbf{K}} | \sigma_- | u_{n\mathbf{K}} \rangle}{(\epsilon_{n\mathbf{K}} - \epsilon_{m\mathbf{K}})(\epsilon_{n\mathbf{K}} - \epsilon_{j\mathbf{K}})} \right], \quad (\text{A2})$$

where $|u_{n\mathbf{K}}\rangle$ and $\epsilon_{n\mathbf{K}}$ are the Bloch state and the eigenvalue, respectively, of $H_0(\mathbf{r})$ at \mathbf{K} , n is the first positive energy band, and $\sigma_{\pm} = \sigma_x \pm i\sigma_y$. The evolution of the couplings α and η is shown in Fig. 5. The higher-order van Hove singularity occurs when the quadratic term α in Eq. (A1) vanishes at $w/(v_F/L) \simeq 1.36$, highlighted by the vertical green line in Fig. 5. The result is a power-law divergence in the density of states $\rho(\epsilon) \sim |\epsilon|^{-1/3}$. By looking at the solutions of $\nabla_{\mathbf{q}} \epsilon_{\pm}(\mathbf{q}) = 0$ (\pm for \mathbf{K} and \mathbf{K}' , respectively), we find that $\mathbf{q} = 0$ is a maximum for $\alpha < 0$, a minimum for $\alpha > 0$, and, finally, a higher-order critical point for $\alpha = 0$. Away from the origin there are three further solutions at $\kappa_{\pm, j} = \mp 2\alpha C_{3z}^{j-1}(1, 0)/3\eta$, which are saddle points. Approaching the higher-order VHS at $\alpha \rightarrow 0$, these three saddle points merge at $\mathbf{q} = 0$, i.e., at \mathbf{K} or \mathbf{K}' .

APPENDIX B: SOLUTION OF THE SADDLE-POINT EQUATIONS

In this section we detail the mean-field solution of the interacting electrons on the surface of the TI subject to the superlattice potential $w(\mathbf{r})$. Minimizing F (5) with respect to the filling n and the magnetic configurations $\mathbf{m}(\mathbf{r})$, we find the

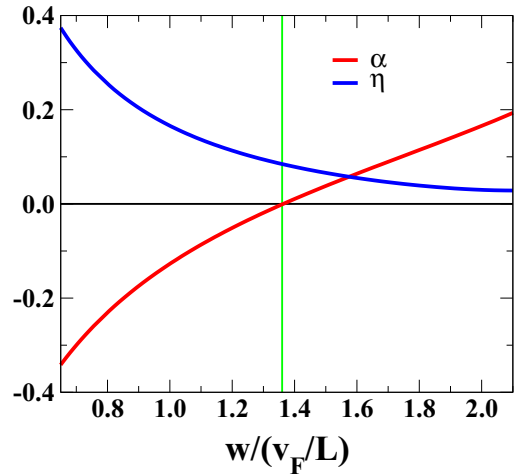


FIG. 5. Parameters α and η of the $\mathbf{k} \cdot \mathbf{p}$ expansion of the dispersion relation around \mathbf{K} . The vanishing of α at $w/(v_F/L) = 1.36$ highlighted by the green line implies a high-order van Hove singularity.

saddle-point equations:

$$\frac{\delta F}{\delta n} = 0 \Rightarrow n = \frac{1}{A} \text{Tr}[(G_0^{-1} + X)^{-1}] \quad (\text{B1})$$

and

$$\frac{\delta F}{\delta s_{\mu j}^*} = 0 \Rightarrow s_{\mu j} = \frac{2}{UA} \text{Tr} \left[\frac{\delta X}{\delta s_{\mu j}^*} (G_0^{-1} + X)^{-1} \right]. \quad (\text{B2})$$

In the main text we show the result of the numerical solution of Eqs. (B1) and (B2), which was obtained as follows. Equations (B1) and (B2) take a simple form in the basis of the eigenstates $|\phi_{n\mathbf{k}}\rangle$ of the Hartree-Fock Hamiltonian in Eq. (6) with eigenvalues $\bar{\epsilon}_{n\mathbf{k}}$:

$$n = \frac{1}{3N} \sum_{n\mathbf{k}} f(\bar{\xi}_{n\mathbf{k}}) - n_0, \quad (\text{B3})$$

where $\bar{\xi}_{n\mathbf{k}} = \bar{\epsilon}_{n\mathbf{k}} - \mu^*$ and $\mu^* = \mu - Un/2$, and

$$s_{\mu j} = \frac{1}{3N} \sum_{n\mathbf{k}} f(\bar{\xi}_{n\mathbf{k}}) \langle \phi_{n\mathbf{k}} | O_{\mu j}^\dagger V^{\delta_j} | \phi_{n\mathbf{k}} \rangle, \quad (\text{B4})$$

where the filling n is measured with respect to the charge neutrality point n_0 , N is the number of points sampling the Brillouin zone, and the factor of three takes into account the size difference between the original and the magnetic Brillouin zone. Moreover, the function $f(\epsilon) = 1/(e^{\beta\epsilon} + 1)$ is the Fermi-Dirac distribution function, and $V^{\mathbf{G}}$ is the sewing matrix satisfying $V_{\mathbf{Q}, \mathbf{Q}+\mathbf{G}}^{\mathbf{G}} = \delta_{\mathbf{Q}, \mathbf{Q}+\mathbf{G}}$, $V^{\mathbf{G}} |\phi_{n\mathbf{k}}\rangle = |\phi_{n\mathbf{k}+\mathbf{G}}\rangle$. The self-consistent equations are performed by a find-root algorithm.

APPENDIX C: SYMMETRIES OF THE FREE ENERGY AND CLASSIFICATION OF MAGNETIC ORDERINGS

In this Appendix we discuss the symmetries of the second-order matrix $\mathcal{M}_{jl}^{\mu\nu}$ and classify the different magnetic orderings according to their symmetry properties. The second-order tensor is constrained by the symmetries in Table I. The

TABLE II. Character table of C_{3v} . E , C_3 , and m represent the conjugation classes of the identity, C_{3z} , and m_y , respectively.

	E	$2C_3$	$3m$
Γ_1	1	1	1
Γ_2	1	1	-1
Γ_3	2	-1	0

threefold rotation about the z axis, $C_{3z} : s_{\mu j} \rightarrow s_{\mu j+1}$, gives $\mathcal{M}_{jl}^{\mu\nu} = \mathcal{M}_{j+1+l+1}^{\mu\nu}$. As a result $\mathcal{M}_{jl}^{\mu\nu}$ is expressed in terms of two three-dimensional matrices: $\Lambda_{\mu\nu} = \mathcal{M}_{j,j}^{\mu\nu}$, $\Omega_{\mu\nu} = \mathcal{M}_{j,j+1}^{\mu\nu}$ while $\mathcal{M}_{j+1,j}^{\mu\nu} = \Omega_{\nu\mu}^*$ since the free energy $F_{(2)}$ is real. In addition, the mirror symmetry m_x (given in Table I) implies that $\Lambda_{\mu\nu}$ is real and symmetric, $\Omega_{\mu\nu} = \Omega_{\nu\mu}$ but with complex elements $\Omega_{\mu\nu}^* \neq \Omega_{\nu\mu}$. Finally, the remaining m_y symmetry imposes that the matrix elements $\Lambda_{\parallel\perp} = 0$ and $\Lambda_{\perp z} = 0$, $\Omega_{\parallel\perp}$ and $\Omega_{\perp z}$ are purely imaginary, while the other components of $\Omega_{\mu\nu}$ are real. The latter constraint implies that the C_{3z} -symmetric spiral- xy order decouples from the 120- xy and out-of-plane orderings. As a result by projecting the second-order free energy $F_{(2)}$ on the C_{3z} -symmetric configuration $s_{\mu j} = \xi U_{\mu}/\sqrt{3}$ we find the expression in the main text Eq. (8) where $L_{\mu\nu} = \Lambda_{\mu\nu} + 2\text{Re}\Omega_{\mu\nu}$.

We now characterize the spectrum of $\mathcal{M}_{jl}^{\mu\nu}$ and we classify the magnetic states with respect to their symmetry behavior under the point-group symmetries of the model. The

magnetic ordering is described by the real order parameter $\mathbf{m}(\mathbf{r}) = \sum_j \mathbf{m}_j e^{i\delta_j \cdot \mathbf{r}} + \text{c.c.}$ which is completely determined by the Fourier amplitudes $\mathbf{m}_j = \sum_{\mu} s_{\mu j} \mathbf{v}_{\mu j}$. The nine magnetic configurations originating from $s_{\mu j}$ are decomposed into one one-dimensional representation Γ_1 , two one-dimensional representations Γ_2 , and three two-dimensional representations Γ_3 given in Table II. The one-dimensional representations Γ_1 and Γ_2 are symmetric under C_{3z} and correspond to equal superpositions of the modulations $\delta_{1,2,3}$. The parity of Γ_1 under m_y is even consistently with the spiral- xy order. On the other hand, Γ_2 is odd under m_y like the 120- xy and out-of-plane orderings. Due to the intrinsic spin-orbit coupling in-plane 120- xy and out-of-plane orderings mix to form the meron lattice state. Finally, we have the two-dimensional representation Γ_3 . Here, we find two eigenstates of C_{3z} characterized by eigenvalues $\omega = e^{2\pi i/3}$ and ω^* and m_y is off-diagonal in this basis. Two-dimensional degeneracy is implied from this symmetry.

In the normal state the two valleys \mathbf{K} and \mathbf{K}' are equally occupied giving rise to a time-reversal-symmetric state with vanishing magnetization. It is important to notice that the two valleys are characterized by nondegenerate Bloch states, $|u_{\mathbf{K}}\rangle$ and $|u_{\mathbf{K}'}\rangle$ (first band above charge neutrality), with opposite mirror eigenvalues. The meron lattice state belonging to Γ_2 breaks the mirror symmetry m_y of \mathbf{K} and \mathbf{K}' and couples $|u_{\mathbf{K}}\rangle$ and $|u_{\mathbf{K}'}\rangle$. The resulting Hartree-Fock orbitals at Γ_m of the magnetic moiré Brillouin zone are eigenstates of the mirror symmetry m_x and correspond to a coherent superposition of the two valleys \mathbf{K} and \mathbf{K}' .

- [1] L. Fu, C. L. Kane, and E. J. Mele, Topological Insulators in Three Dimensions, *Phys. Rev. Lett.* **98**, 106803 (2007).
- [2] J. E. Moore and L. Balents, Topological invariants of time-reversal-invariant band structures, *Phys. Rev. B* **75**, 121306(R) (2007).
- [3] R. Roy, Topological phases and the quantum spin Hall effect in three dimensions, *Phys. Rev. B* **79**, 195322 (2009).
- [4] M. König, S. Wiedmann, C. Brüne, A. Roth, H. Buhmann, L. W. Molenkamp, X.-L. Qi, and S.-C. Zhang, Quantum spin Hall insulator state in HgTe quantum wells, *Science* **318**, 766 (2007).
- [5] L. Fu, Hexagonal warping effects in the surface states of the topological insulator Bi_2Te_3 , *Phys. Rev. Lett.* **103**, 266801 (2009).
- [6] D. Hsieh, D. Qian, L. Wray, Y. Xia, Y. S. Hor, R. J. Cava, and M. Z. Hasan, A topological Dirac insulator in a quantum spin Hall phase (experimental realization of a 3D topological insulator), [arXiv:0910.2420](https://arxiv.org/abs/0910.2420).
- [7] D. Hsieh, Y. Y. Xia, D. Qian, L. A. Wray, J. H. Dil, F. Meier, J. Osterwalder, L. Patthey, J. G. Checkelsky, N. P. Ong, A. V. Fedorov, H. I. Lin, A. Bansil, D. Grauer, Y. S. Hor, R. J. Cava, and M. Z. Hasan, A tunable topological insulator in the spin helical Dirac transport regime, *Nature (London)* **460**, 1101 (2009).
- [8] Y. L. Chen, J. G. Analytis, J.-H. Chu, Z. K. Liu, S.-K. Mo, X. L. Qi, H. J. Zhang, D. H. Lu, X. Dai, Z. Fang, S. C. Zhang, I. R. Fisher, Z. Hussain, and Z.-X. Shen, Experimental realization of a three-dimensional topological insulator, Bi_2Te_3 , *Science* **325**, 178 (2009).
- [9] Y. Xia, D. Qian, D. Hsieh, L. A. Wray, A. Pal, H. Lin, A. Bansil, D. Grauer, Y. S. Hor, R. J. Cava, and M. Z. Hasan, Observation of a large-gap topological-insulator class with a single Dirac cone on the surface, *Nat. Phys.* **5**, 398 (2009).
- [10] C. Brüne, C. X. Liu, E. G. Novik, E. M. Hankiewicz, H. Buhmann, Y. L. Chen, X. L. Qi, Z. X. Shen, S. C. Zhang, and L. W. Molenkamp, Quantum Hall Effect from the Topological Surface States of Strained Bulk HgTe, *Phys. Rev. Lett.* **106**, 126803 (2011).
- [11] S. Souma, K. Kosaka, T. Sato, M. Komatsu, A. Takayama, T. Takahashi, M. Kriener, K. Segawa, and Y. Ando, Direct Measurement of the Out-of-Plane Spin Texture in the Dirac-Cone Surface State of a Topological Insulator, *Phys. Rev. Lett.* **106**, 216803 (2011).
- [12] J.-H. Jiang and S. Wu, Spin susceptibility and helical magnetic order at the edges/surfaces of topological insulators due to Fermi surface nesting, *Phys. Rev. B* **83**, 205124 (2011).
- [13] Y. Baum and A. Stern, Magnetic instability on the surface of topological insulators, *Phys. Rev. B* **85**, 121105(R) (2012).
- [14] Y. Baum and A. Stern, Density-waves instability and a skyrmion lattice on the surface of strong topological insulators, *Phys. Rev. B* **86**, 195116 (2012).
- [15] D. J. J. Marchand and M. Franz, Lattice model for the surface states of a topological insulator with applications to magnetic and exciton instabilities, *Phys. Rev. B* **86**, 155146 (2012).
- [16] M. J. Schmidt, Strong correlations at topological insulator surfaces and the breakdown of the bulk-boundary correspondence, *Phys. Rev. B* **86**, 161110(R) (2012).

- [17] M. Sitte, A. Rosch, and L. Fritz, Interaction effects on almost flat surface bands in topological insulators, *Phys. Rev. B* **88**, 205107 (2013).
- [18] D. Mendler, P. Kotetes, and G. Schön, Magnetic order on a topological insulator surface with warping and proximity-induced superconductivity, *Phys. Rev. B* **91**, 155405 (2015).
- [19] J. Cano, S. Fang, J. H. Pixley, and J. H. Wilson, Moiré superlattice on the surface of a topological insulator, *Phys. Rev. B* **103**, 155157 (2021).
- [20] T. Wang, N. F. Q. Yuan, and L. Fu, Moiré Surface States and Enhanced Superconductivity in Topological Insulators, *Phys. Rev. X* **11**, 021024 (2021).
- [21] N. Gao, S. G. Je, M. Y. Im, J. W. Choi, M. Yang, Q. Li, T. Y. Wang, S. Lee, H. S. Han, K. S. Lee, W. Chao, C. Hwang, J. Li, and Z. Q. Qiu, Creation and annihilation of topological meron pairs in in-plane magnetized films, *Nat. Commun.* **10**, 5603 (2019).
- [22] S. Mühlbauer, B. Binz, F. Jonietz, C. Pfleiderer, A. Rosch, A. Neubauer, R. Georgii, and P. Boni, Skyrmion lattice in a chiral magnet, *Science* **323**, 915 (2009).
- [23] C. Pappas, E. Lelièvre-Berna, P. Falus, P. M. Bentley, E. Moskvin, S. Grigoriev, P. Fouquet, and B. Farago, Chiral Paramagnetic Skyrmion-like Phase in MnSi, *Phys. Rev. Lett.* **102**, 197202 (2009).
- [24] A. Neubauer, C. Pfleiderer, B. Binz, A. Rosch, R. Ritz, P. G. Niklowitz, and P. Böni, Topological Hall effect in the α phase of MnSi, *Phys. Rev. Lett.* **102**, 186602 (2009).
- [25] N. Nagaosa and Y. Tokura, Topological properties and dynamics of magnetic skyrmions, *Nat. Nanotechnol.* **8**, 899 (2013).
- [26] S. Heinze, K. von Bergmann, M. Menzel, J. Brede, A. Kubetzka, R. Wiesendanger, G. Bihlmayer, and S. Blügel, Spontaneous atomic-scale magnetic skyrmion lattice in two dimensions, *Nat. Phys.* **7**, 713 (2011).
- [27] N. Romming, C. Hanneken, M. Menzel, J. E. Bickel, B. Wolter, K. von Bergmann, A. Kubetzka, and R. Wiesendanger, Writing and deleting single magnetic skyrmions, *Science* **341**, 636 (2013).
- [28] I. Gross, W. Akhtar, A. Hrabec, J. Sampaio, L. J. Martínez, S. Chouaieb, B. J. Shields, P. Maletinsky, A. Thiaville, S. Rohart, and V. Jacques, Skyrmion morphology in ultrathin magnetic films, *Phys. Rev. Mater.* **2**, 024406 (2018).
- [29] S. Seki, X. Z. Yu, S. Ishiwata, and Y. Tokura, Observation of skyrmions in a multiferroic material, *Science* **336**, 198 (2012).
- [30] X. Yu, M. Mostovoy, Y. Tokunaga, W. Zhang, K. Kimoto, Y. Matsui, Y. Kaneko, N. Nagaosa, and Y. Tokura, Magnetic stripes and skyrmions with helicity reversals, *Proc. Natl. Acad. Sci. USA* **109**, 8856 (2012).
- [31] X. Z. Yu, W. Koshibae, Y. Tokunaga, K. Shibata, Y. Taguchi, N. Nagaosa, and Y. Tokura, Transformation between meron and skyrmion topological spin textures in a chiral magnet, *Nature (London)* **564**, 95 (2018).
- [32] S. Gao, H. D. Rosales, F. A. G. Albarracín, V. Tsurkan, G. Kaur, T. Fennell, P. Steffens, M. Boehm, P. Čermák, A. Schneidewind, E. Ressouche, D. C. Cabra, C. Rüegg, and O. Zaharko, Fractional antiferromagnetic skyrmion lattice induced by anisotropic couplings, *Nature (London)* **586**, 37 (2020).
- [33] S. Dovic, H. Ling, T. Pereg-Barnea, and A. Paramekanti, Magnetic skyrmion crystal at a topological insulator surface, *Phys. Rev. B* **105**, 035156 (2022).
- [34] K. Nomura and N. Nagaosa, Electric charging of magnetic textures on the surface of a topological insulator, *Phys. Rev. B* **82**, 161401(R) (2010).
- [35] H. M. Hurst, D. K. Efimkin, J. Zang, and V. Galitski, Charged skyrmions on the surface of a topological insulator, *Phys. Rev. B* **91**, 060401 (2015).
- [36] K. L. Tiwari, J. Lavoie, T. Pereg-Barnea, and W. A. Coish, Tunable skyrmion-skyrmion binding on the surface of a topological insulator, *Phys. Rev. B* **100**, 125414 (2019).
- [37] N. Paul and L. Fu, Topological magnetic textures in magnetic topological insulators, *Phys. Rev. Res.* **3**, 033173 (2021).
- [38] C. Forsythe, X. Zhou, K. Watanabe, T. Taniguchi, A. Pasupathy, P. Moon, M. Koshino, P. Kim, and C. R. Dean, Band structure engineering of 2D materials using patterned dielectric superlattices, *Nat. Nanotechnol.* **13**, 566 (2018).
- [39] Y. Li, S. Dietrich, C. Forsythe, T. Taniguchi, K. Watanabe, P. Moon, and C. R. Dean, Anisotropic band flattening in graphene with one-dimensional superlattices, *Nat. Nanotechnol.* **16**, 525 (2021).
- [40] C.-L. Song, Y.-L. Wang, Y.-P. Jiang, Y. Zhang, C.-Z. Chang, L. Wang, K. He, X. Chen, J.-F. Jia, Y. Wang, Z. Fang, X. Dai, X.-C. Xie, X.-L. Qi, S.-C. Zhang, Q.-K. Xue, and X. Ma, Topological insulator Bi_2Se_3 thin films grown on double-layer graphene by molecular beam epitaxy, *Appl. Phys. Lett.* **97**, 143118 (2010).
- [41] Y.-Z. Chou, J. Cano, and J. H. Pixley, Band manipulation and spin texture in interacting moiré helical edges, *Phys. Rev. B* **104**, L201113 (2021).
- [42] Z. Liu, H. Wang, and J. Wang, Magnetic moiré surface states and flat Chern band in topological insulators, *Phys. Rev. B* **106**, 035114 (2022).
- [43] L.-k. Shi, J. Ma, and J. C. Song, Gate-tunable flat bands in van der Waals patterned dielectric superlattices, *2D Mater.* **7**, 015028 (2020).
- [44] J. Zhang, C. Triola, and E. Rossi, Proximity Effect in Graphene–Topological–Insulator Heterostructures, *Phys. Rev. Lett.* **112**, 096802 (2014).
- [45] K. Schouteden, Z. Li, T. Chen, F. Song, B. Partoens, C. Van Haesendonck, and K. Park, Moiré superlattices at the topological insulator Bi_2Te_3 , *Sci. Rep.* **6**, 20278 (2016).
- [46] A. Vargas, F. Liu, C. Lane, D. Rubin, I. Bilgin, Z. Hennighausen, M. DeCapua, A. Bansil, and S. Kar, Tunable and laser-reconfigurable 2D heterocrystals obtained by epitaxial stacking of crystallographically incommensurate Bi_2Se_3 and MoS_2 atomic layers, *Sci. Adv.* **3**, e1601741 (2017).
- [47] Z. Hennighausen, C. Lane, A. Benabbas, K. Mendez, M. Eggenberger, P. M. Champion, J. T. Robinson, A. Bansil, and S. Kar, Oxygen-induced in situ manipulation of the interlayer coupling and exciton recombination in $\text{Bi}_2\text{Se}_3/\text{MoS}_2$ 2D heterostructures, *ACS Appl. Mater. Interfaces* **11**, 15913 (2019).
- [48] Z. Hennighausen, C. Lane, I. G. Buda, V. K. Mathur, A. Bansil, and S. Kar, Evidence of a purely electronic two-dimensional lattice at the interface of TMD/ Bi_2Se_3 heterostructures, *Nanoscale* **11**, 15929 (2019).
- [49] A. Dunbrack and J. Cano, Magic angle conditions for twisted 3D topological insulators, *Phys. Rev. B* **106**, 075142 (2022).
- [50] E. Tang and L. Fu, Strain-induced partially flat band, helical snake states and interface superconductivity in topological crystalline insulators, *Nat. Phys.* **10**, 964 (2014).

- [51] Y. Liu, Y. Li, S. Rajput, D. Gilks, L. Lari, P. Galindo, M. Weinert, V. Lazarov, and L. Li, Tuning Dirac states by strain in the topological insulator Bi_2Se_3 , *Nat. Phys.* **10**, 294 (2014).
- [52] N. F. Q. Yuan and L. Fu, Classification of critical points in energy bands based on topology, scaling, and symmetry, *Phys. Rev. B* **101**, 125120 (2020).
- [53] N. F. Q. Yuan, H. Isobe, and L. Fu, Magic of high-order van Hove singularity, *Nat. Commun.* **10**, 5769 (2019).
- [54] A. Chandrasekaran, A. Shtyk, J. J. Betouras, and C. Chamon, Catastrophe theory classification of Fermi surface topological transitions in two dimensions, *Phys. Rev. Res.* **2**, 013355 (2020).
- [55] D. Guerci, P. Simon, and C. Mora, Higher-order van Hove singularity in magic-angle twisted trilayer graphene, *Phys. Rev. Res.* **4**, L012013 (2022).
- [56] C. Mudry, *Lecture Notes on Field Theory in Condensed Matter Physics* (World Scientific, 2014).
- [57] E. Fradkin, *Field Theories of Condensed Matter Physics*, 2nd ed. (Cambridge University Press, 2013).
- [58] A. Altland and B. D. Simons, *Condensed Matter Field Theory*, 2nd ed. (Cambridge University Press, 2010).
- [59] E. C. Stoner, Collective electron ferromagnetism, *Proc. R. Soc. London A* **165**, 372 (1938).
- [60] G. Litak, A. Martin, B. Györfy, J. Annett, and K. Wysokiński, Van Hove singularity and d -wave pairing in disordered superconductors, *Physica C: Superconductivity* **309**, 257 (1998).
- [61] J. H. Wilson, Y. Fu, S. Das Sarma, and J. H. Pixley, Disorder in twisted bilayer graphene, *Phys. Rev. Res.* **2**, 023325 (2020).
- [62] A. Chandrasekaran and J. J. Betouras, Effect of disorder on density of states and conductivity in higher-order van Hove singularities in two-dimensional bands, *Phys. Rev. B* **105**, 075144 (2022).
- [63] K. Sawada and N. Nagaosa, Optical Magnetoelectric Effect in Multiferroic Materials: Evidence for a Lorentz Force Acting on a Ray of Light, *Phys. Rev. Lett.* **95**, 237402 (2005).
- [64] C. Ederer and N. A. Spaldin, Towards a microscopic theory of toroidal moments in bulk periodic crystals, *Phys. Rev. B* **76**, 214404 (2007).
- [65] S. Bhowal and N. A. Spaldin, Magnetoelectric Classification of Skyrmions, *Phys. Rev. Lett.* **128**, 227204 (2022).
- [66] S. Zhong, J. E. Moore, and I. Souza, Gyrotropic Magnetic Effect and the Magnetic Moment on the Fermi Surface, *Phys. Rev. Lett.* **116**, 077201 (2016).
- [67] J. Ma and D. A. Pesin, Chiral magnetic effect and natural optical activity in metals with or without Weyl points, *Phys. Rev. B* **92**, 235205 (2015).
- [68] X. Yu, Y. Onose, N. Kanazawa, J. Park, J. Han, Y. Matsui, N. Nagaosa, and Y. Tokura, Real-space observation of a two-dimensional skyrmion crystal, *Nature (London)* **465**, 901 (2010).
- [69] Y. Dovzhenko, F. Casola, S. Schlotter, T. X. Zhou, F. Büttner, R. L. Walsworth, G. S. D. Beach, and A. Yacoby, Magnetostatic twists in room-temperature skyrmions explored by nitrogen-vacancy center spin texture reconstruction, *Nat. Commun.* **9**, 2712 (2018).
- [70] S. V. Grigoriev, V. A. Dyadkin, D. Menzel, J. Schoenes, Y. O. Chetverikov, A. I. Okorokov, H. Eckerlebe, and S. V. Maleyev, Magnetic structure of $\text{Fe}_{1-x}\text{Co}_x\text{Si}$ in a magnetic field studied via small-angle polarized neutron diffraction, *Phys. Rev. B* **76**, 224424 (2007).
- [71] S. Seki, J.-H. Kim, D. S. Inosov, R. Georgii, B. Keimer, S. Ishiwata, and Y. Tokura, Formation and rotation of skyrmion crystal in the chiral-lattice insulator Cu_2OSeO_3 , *Phys. Rev. B* **85**, 220406(R) (2012).
- [72] S. V. Grigoriev, D. Chernyshov, V. A. Dyadkin, V. Dmitriev, S. V. Maleyev, E. V. Moskvina, D. Menzel, J. Schoenes, and H. Eckerlebe, Crystal Handedness and Spin Helix Chirality in $\text{Fe}_{1-x}\text{Co}_x\text{Si}$, *Phys. Rev. Lett.* **102**, 037204 (2009).
- [73] H. Wilhelm, M. Baenitz, M. Schmidt, U. K. Röbler, A. A. Leonov, and A. N. Bogdanov, Precursor Phenomena at the Magnetic Ordering of the Cubic Helimagnet FeGe , *Phys. Rev. Lett.* **107**, 127203 (2011).
- [74] M. Hirschberger, T. Nakajima, S. Gao, L. Peng, A. Kikkawa, T. Kurumaji, M. Kriener, Y. Yamasaki, H. Sagayama, H. Nakao, K. Ohishi, K. Kakurai, Y. Taguchi, X. Yu, T. Arima, and Y. Tokura, Skyrmion phase and competing magnetic orders on a breathing kagomé lattice, *Nat. Commun.* **10**, 5831 (2019).
- [75] R. Brearton, L. Turnbull, J. Verezhak, G. Balakrishnan, P. Hatton, G. Laan, and T. Hesjedal, Deriving the skyrmion Hall angle from skyrmion lattice dynamics, *Nat. Commun.* **12**, 2723 (2021).
- [76] B. Huang, G. Clark, E. Navarro-Moratalla, D. R. Klein, R. Cheng, K. L. Seyler, D. Zhong, E. Schmidgall, M. A. McGuire, D. H. Cobden, W. Yao, D. Xiao, P. Jarillo-Herrero, and X. Xu, Layer-dependent ferromagnetism in a van der Waals crystal down to the monolayer limit, *Nature (London)* **546**, 270 (2017).
- [77] J. Liu, A. Singh, B. Kuerbanjiang, C. H. W. Barnes, and T. Hesjedal, Kerr effect anomaly in magnetic topological insulator superlattices, *Nanotechnology* **31**, 434001 (2020).
- [78] T. Song, X. Cai, M. W.-Y. Tu, X. Zhang, B. Huang, N. P. Wilson, K. L. Seyler, L. Zhu, T. Taniguchi, K. Watanabe, M. A. McGuire, D. H. Cobden, D. Xiao, W. Yao, and X. Xu, Giant tunneling magnetoresistance in spin-filter van der Waals heterostructures, *Science* **360**, 1214 (2018).
- [79] J. Ye, Y. B. Kim, A. J. Millis, B. I. Shraiman, P. Majumdar, and Z. Tešanović, Berry Phase Theory of the Anomalous Hall Effect: Application to Colossal Magnetoresistance Manganites, *Phys. Rev. Lett.* **83**, 3737 (1999).
- [80] Y. Taguchi, Y. Oohara, H. Yoshizawa, N. Nagaosa, and Y. Tokura, Spin chirality, Berry phase, and anomalous Hall effect in a frustrated ferromagnet, *Science* **291**, 2573 (2001).
- [81] P. Bruno, V. K. Dugaev, and M. Taillefumier, Topological Hall Effect and Berry Phase in Magnetic Nanostructures, *Phys. Rev. Lett.* **93**, 096806 (2004).
- [82] M. Onoda, G. Tatara, and N. Nagaosa, Anomalous Hall effect and skyrmion number in real and momentum spaces, *J. Phys. Soc. Jpn.* **73**, 2624 (2004).
- [83] B. Binz and A. Vishwanath, Chirality induced anomalous-Hall effect in helical spin crystals, *Phys. B: Condens. Matter* **403**, 1336 (2008).
- [84] N. Nagaosa and Y. Tokura, Emergent electromagnetism in solids, *Phys. Scr.* **T146**, 014020 (2012).
- [85] T. Schulz, R. Ritz, A. Bauer, M. Halder, M. Wagner, C. Franz, C. Pfleiderer, K. Everschor, M. Garst, and A. Rosch, Emergent electrodynamics of skyrmions in a chiral magnet, *Nat. Phys.* **8**, 301 (2012).
- [86] K. Shimizu, S. Okumura, Y. Kato, and Y. Motome, Spin moiré engineering of topological magnetism and emergent electromagnetic fields, *Phys. Rev. B* **103**, 184421 (2021).

- [87] Y. Guan, O. V. Yazyev, and A. Kruchkov, Unconventional flat Chern bands and $2e$ charges in skyrmionic moiré superlattices, [arXiv:2111.10410](#).
- [88] J. Wang, J. Zang, J. Cano, and A. J. Millis, Staggered pseudo magnetic field in twisted transition metal dichalcogenides: Physical origin and experimental consequences, [arXiv:2110.14570](#).
- [89] J. Zang, J. Wang, J. Cano, and A. J. Millis, Hartree-fock study of the moiré Hubbard model for twisted bilayer transition metal dichalcogenides, *Phys. Rev. B* **104**, 075150 (2021).
- [90] A. Fert, V. Cros, and J. Sampaio, Skyrmions on the track, *Nat. Nanotechnol.* **8**, 152 (2013).
- [91] A. Fert, N. Reyren, and V. Cros, Magnetic skyrmions: Advances in physics and potential applications, *Nat. Rev. Mater.* **2**, 17031 (2017).
- [92] X. Zhang, M. Ezawa, and Y. Zhou, Magnetic skyrmion logic gates: Conversion, duplication and merging of skyrmions, *Sci. Rep.* **5**, 9400 (2015).
- [93] X. Zhang, Y. Zhou, K. Mee Song, T.-E. Park, J. Xia, M. Ezawa, X. Liu, W. Zhao, G. Zhao, and S. Woo, Skyrmion-electronics: Writing, deleting, reading and processing magnetic skyrmions toward spintronic applications, *J. Phys.: Condens. Matter* **32**, 143001 (2020).
- [94] Z. Bi, N. F. Q. Yuan, and L. Fu, Designing flat bands by strain, *Phys. Rev. B* **100**, 035448 (2019).
- [95] L. Balents, General continuum model for twisted bilayer graphene and arbitrary smooth deformations, *SciPost Phys.* **7**, 048 (2019).
- [96] W.-Y. He, D. Goldhaber-Gordon, and K. T. Law, Giant orbital magnetoelectric effect and current-induced magnetization switching in twisted bilayer graphene, *Nat. Commun.* **11**, 1650 (2020).
- [97] N. N. T. Nam and M. Koshino, Lattice relaxation and energy band modulation in twisted bilayer graphene, *Phys. Rev. B* **96**, 075311 (2017).